Tribology International 177 (2023) 107954

Contents lists available at ScienceDirect

Tribology International

journal homepage: www.elsevier.com/locate/triboint

Transient rotordynamic thermal bow (Morton effect) modeling in flexure-pivot tilting pad bearing systems

Xiaomeng Tong [a], Weiqing Xu [a], Yan Shi [a,*], Maolin Cai [a], Alan Palazzolo [b]

[a] School of Automation Science and Electrical Engineering, Beihang University, Beijing 100191, China
[b] Department of Mechanical Engineering, Texas A&M University, College Station, TX 77840, USA

ARTICLE INFO

Keywords:
Morton effect
Thermal bow
Flexure-pivot bearings
Thermo-elasto-hydrodynamics

ABSTRACT

The Morton effect (ME) is a thermally induced rotodynamic instability problem frequently reported in the fluid film bearing system. The temperature difference across the journal circumference may cause large spiral, synchronous vibration. Earlier ME modeling approaches rarely focus on the flexure-pivot bearing (FPB), significantly disproportionate to its wide application. Hereby, the transient ME prediction algorithm is proposed based on a high-fidelity thermo-elasto-hydrodynamic FPB model. A hybrid finite element analysis is adopted to evaluate the entire rotor thermal bow profile including the rotor midspan. The algorithm is benchmarked with experiments and applied to a realistic compressor model. Simulations confirm the proneness of the FPB system to the ME instability, and reveal the ME sensitivity to the bearing-rotor configuration and operation conditions.

1. Introduction

The flexure-pivot tilting pad journal bearing (FPTPJB) consists of a one-piece pad-web-housing design machined by the electrical discharge process. It is featured with relatively low cross-coupling coefficients and great stability characteristics, and meanwhile, eliminates the limitations of the traditional tilting pad bearing, such as stack-up tolerance, pivot wear, etc. The cost-effective manufacture plus the superior rotodynamic performance helps FPTPJBs gain wide popularity in industries.

The general interest of the FPTPJB research concentrates on the dynamic coefficients. In 1996, San Andres [1] presented the thermal analysis of the flexure-pivot hybrid bearings for cryogenic applications and correlated the predictions with the measured dynamic coefficients. A turbulent bulk-flow model was adopted, and the web was assumed to produce only rotational stiffness. In 1998, the first flexible pad-web model was provided by Kepple et al. [2], and the research focused on the web stress and fatigue life of a single pad-web model. In 2006, Al-Ghasem and Childs [3,4] conducted experiments with a four-pad FPTPJB for a range of rotor speeds and bearing unit loadings. The measured dynamic coefficients were compared to predictions using an isothermal and bulk-flow Navier-Stokes model. In 2017, Suh [5] presented a three-dimensional (3D) iso-viscous elasto-hydrodynamics (EHD) model without considering the thermal expansion of the solids. The pad and web elastic deformation were included and the EHD analysis was proven to offer satisfactory predictions of the dynamic coefficients. In 2020, Vannini et al. [6] tested a four-pad FPTPJB with a large diameter of 280 mm at various loadings and speeds, and the measured dynamic coefficients agreed well with the thermo-hydrodynamic (THD) prediction tool. The tool employed two-dimensional (2D) profiles for pressure and temperature, and used a curved beam element to approximate the mechanical and thermal deformation of the pads.

Meanwhile, the past two decades see rapidly increasing cases of fluid film bearing induced thermal instability in the turbomachinery equipment, and a lot of them are attributed to the journal asymmetric heating by the fluid film bearings, also termed the "Morton effect" [7,8]. The non-uniform viscous shearing in the lubricant, coinciding with the rotor synchronous vibration, can cause high temperature difference across the journal circumference, i.e., journal ΔT, which induces the rotor thermal bow and triggers excessive vibration. The Morton effect (ME) has been widely reported in various rotor and bearing configurations [9], and the accurate ME prediction is beyond the capability of the traditional rotordynamics software [10], posing significant risks for the turbomachinery equipment.

Accurate ME prediction requires a THD or a more sophisticated TEHD (Thermo-elasto-hydrodynamics) bearing model, which also takes account of the bearing and shaft elastic/thermal deformation based on the THD analysis. Keogh and Morton [11,12] adopted the short-bearing

* Corresponding author.
E-mail address: shiyan@buaa.edu.cn (Y. Shi).

https://doi.org/10.1016/j.triboint.2022.107954
Received 26 May 2022; Received in revised form 12 September 2022; Accepted 25 September 2022
Available online 28 September 2022

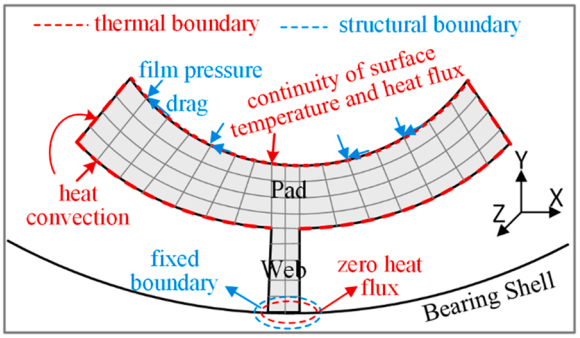

Fig. 1. Boundary conditions for pad thermal and structural analysis.

theory and analyzed the rotor thermal bow with Nyquist graphs to solve the stability problem in the frequency domain. Gomiciaga and Keogh [13] applied computational fluid dynamics (CFD) to analyze the dynamic flow and heat transport in the lubricant and obtain the asymmetric heat into the journal by orbit time-averaging. The procedure was applied to a two-inlet circular bearing over a range of rotational speeds. Balbahadur and Kirk [14] employed the imbalance threshold criterion to replace the frequency domain analysis, and tested the algorithm in both plain journal bearings and tilting pad bearings. Murphy and Lorenz [15,16], deJongh and Morton [17] adopted a simplified ME approach, where the interactions between vibration, imbalance and journal ΔT were linearized with sensitivity coefficients. The simplified approach correctly predicted the ME instability in partial arc bearings [16], sleeve bearings [15], and tilting pad bearings [17]. Panara et al. [18] and Rindi et al. [19] proposed an efficient iterative approach for the thermal instability analysis, and the algorithm was successfully benchmarked with experiments by a tilting pad bearing testing rig. Palazzolo and his colleagues [20–24] proposed the transient ME prediction algorithm based on the high-fidelity TEHD bearing model, and verified the theories by the measured journal ΔT inside a tilting pad bearing [25]. Plantegenet and Arghir [26,27] conducted the ME experiments with various rotor geometries, and both the sleeve bearing and the FPTPJB were tested with strong ME observed. Shin et al. [28] extended the transient ME algorithm from the tilting pad bearing system to the FPTPJB system, and conducted the parametric study of a single-overhung rotor supported by one non-ME bearing and one FPTPJB. The non-ME bearing was assigned a constant dynamic coefficient and did not contribute to any thermal effect or rotor thermal bow. Simulations demonstrated that the FPTPJB parameters may have a major effect on the ME severity.

Despite the significant efforts to improve the ME algorithm, most theoretical research focuses on the classic tilting pad bearings, the fixed pad bearings, or the sleeve bearings. Relevant studies precisely targeting the FPTPJB-induced ME instability are still insufficient, significantly disproportionate to the wide application of FPTPJBs in the industry. Hereby, the current research is proposed to connect the dots between the ME and the FPTPJBs and offers practical guidelines to mitigate the ME based on the simulations. A more general ME model is proposed, which can tackle multiple ME-FPTPJB bearings with a relatively complex double-overhung rotor configuration. The model is capable to evaluate the entire rotor thermal bow induced by multiple bearings including both overhung and midspan rotor locations and thus can better adapt to the miscellaneous turbomachinery applications. The manuscript is organized as follows: Section 2 introduces the TEHD model of the FPTPJBs, Section 3 details the hybrid finite element analysis (FEA) to calculate the rotor thermal bow, Section 4 discusses the algorithm workflow and the experimental benchmark, and Section 5 details the ME response in a realistic compressor, with conclusions given in Section 6.

2. TEHD analysis

2.1. 3D structural and thermal models

The conventional FPTPJB dynamics model includes a rigid pad, attached with a rotational stiffness representing the web flexibility. This model ignores pad flexibility, pivot radial flexibility, and the coupling flexibility between the pad and web. The current approach employs a flexible pad and web, modeled with 3D structural finite elements to calculate the elastic and thermal deformation in the circumferential, radial, and axial directions. Fig. 1 illustrates the thermal and structural boundary conditions for a pad, where the bottom web nodes are assumed fully fixed in the structural model, and thermally insulated from the bearing shell. This allows each pad to be analyzed individually by decoupling it from the other pads and neglecting the bearing shell. This approach facilitates the multiple-bearing transient ME simulation with a much higher computational efficiency than using a thermally and structurally coupled model, consisting of the bearing shell and all pads in one piece. The accuracy of the simplified models proves to be satisfactory in Section 4.2. The overall pad deformation, which plays a major role in updating the film thickness, is formed from a linear superposition of the elastic deflection and the thermal expansion. The hydrodynamic pressure and friction drag on the pad inner surface in Fig. 1 will tilt and bend the pad, similar to a traditional tilting pad bearing, and the pad will also deflect in the -Y direction due to the web compression. The pad temperature rise will thermally expand the pad inwards, i.e., in the +Y direction, reducing the designed bearing clearance. The modal truncation method is employed with an optimized number of modes, to reduce the computational burden associated with the 3D pad dynamics solver in the transient analysis The governing equation of the reduced-order pad dynamics is listed in Eq. (1), where $M_{p,rom}$, $K_{p,rom}, F_{p,rom}$ are the pad mass, stiffness, and force matrices of the reduced-order model, M_p, K_p, F_p are the pad mass, stiffness, and force matrices of the original model, V consists of a selected number of pad eigenmodes, and Y_p is the state variable with modal coordinates. The number of modes in the modal truncation method is selected to balance accuracy and efficiency and is detailed in Section 4.2.

$$M_{p,rom}\ddot{Y}_p + K_{p,rom}Y_p = F_{p,rom} \tag{1}$$

where, $M_{p,rom} = V^T M_p V, K_{p,rom} = V^T K_p V, \quad F_{p,rom} = V^T F_p$.

Pad and rotor temperature T are solved with the 3D, transient heat conduction Eq. (2) with FEA, where x, y, z are the circumferential, radial, and axial axis, ρ, c, k are the density, heat capacity, and heat

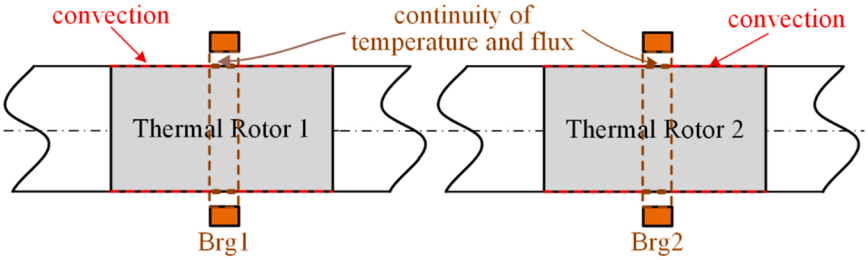

Fig. 2. Boundary conditions for the rotor thermal model.

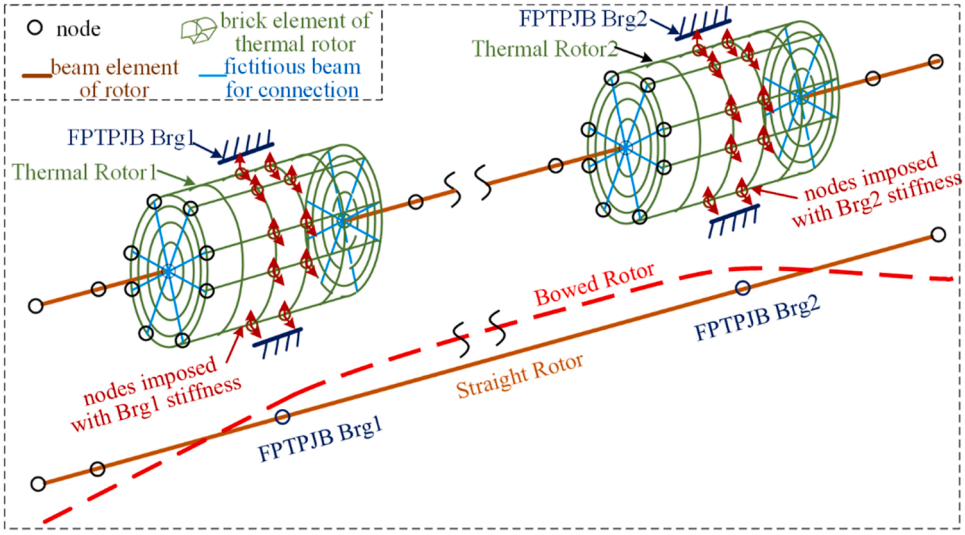

Fig. 3. Schematics of the hybrid finite element method.

conductivity coefficient. The thermal boundary conditions of the bearing model are shown in Fig. 1. Heat convection boundaries are prescribed on the pad surfaces exposed to the ambient, and since the pad surfaces are usually surrounded by lubricating oil, the ambient temperature of the convection boundaries is assumed to be the supply oil temperature for simplicity. The inner pad surface is prescribed with the continuity of temperature and heat flux, as shown in Eq. (3), where the subscripts of "solid" and "film" refer to the pad/journal and the fluid film, respectively, and r is in the journal radial direction. The rotor thermal model is illustrated in Fig. 2. Within the bearing length, the journal-film interface is prescribed with continuity of temperature and heat flux, and the rotor surfaces exposed to the ambient air are imposed with a heat convection boundary condition. The shaft thermal model is truncated near to the bearing by assuming the related temperature gradients occur only locally to the bearing. This facilitates a practical approach for managing computational time. The shaft thermal model is termed the "thermal rotor", which is set to seven times the bearing length, to balance the accuracy and computational cost [21,29].

$$\frac{\partial^2 T}{\partial x^2}+\frac{\partial^2 T}{\partial y^2}+\frac{\partial^2 T}{\partial z^2}=\frac{\rho c}{k}\frac{\partial T}{\partial t} \tag{2}$$

$$\left\{\begin{array}{c} T_{solid}=T_{film} \\ k_{solid}\partial T_{solid}/\partial r=k_{film}\partial T_{film}/\partial r \end{array}\right\} \tag{3}$$

2.2. Energy equation

The 3D energy equation in Eq. (4) is solved with FEA to predict the fluid film temperature in the circumferential x, thickness y, and axial z directions, and c_p is the heat capacity of the fluid film. The film viscosity μ is updated using the exponential temperature-viscosity relation, and then used in the Reynolds equation solver in each time step to obtain the nodal velocity components u, w in the x and z direction, and the film pressure P. The solution of the Reynolds equation is elucidated in the authors' earlier publications [21,29]. The 3D energy equation improves the simplified 2D version [20], which neglects the axial film temperature variation and can over-predict the journal ΔT as well as the thermal bow response. The inlet oil temperature at the pad leading edge is estimated by the classic oil mixing model, which uses a lumped mixing coefficient to simplify the sophisticated mixing process of the cool fresh oil from the supply system and the hot carryover oil exiting from the previous pad [20,21].

$$\rho c_p\left(\frac{\partial T}{\partial t}+u\frac{\partial T}{\partial x}+w\frac{\partial T}{\partial z}\right)=k\left(\frac{\partial^2 T}{\partial x^2}+\frac{\partial^2 T}{\partial y^2}+\frac{\partial^2 T}{\partial z^2}\right)+\left(u\frac{\partial P}{\partial x}+w\frac{\partial P}{\partial z}\right)+\Phi \tag{4}$$

where, $\Phi=\mu[(\frac{\partial u}{\partial y})^2+(\frac{\partial w}{\partial y})^2]$.

Due to the elastic/thermal deformation of the solids, the hot bearing clearance will differ from the designed bearing clearance C_b. The film thickness h at the pad inner surface (x,y) is expressed in Eq. (5), where (x_j,y_j) is the transient journal center, R_j is the journal radius, $h_{\Delta T,p}$ and $h_{\Delta T,j}$ are the pad/journal thermal expansion. Note that (x,y) already includes the pad elastic deformation from the pad dynamics/structural solver, and (x_j,y_j) is provided by the transient rotordynamics solver.

$$h(x,y,t)=\sqrt[2]{(x(t)-x_j(t))^2+(y(t)-y_j(t))^2}-R_j-h_{\Delta T,p}(x,y,t)-h_{\Delta T,j}(x,y,t) \tag{5}$$

3. Rotor thermal bow and thermal imbalance

3.1. Rotor thermal bow

The rotor thermal bow prediction is a fundamental step in analyzing the ME response. Earlier studies can be generally categorized into two groups. Group one adopted a linear formula by assuming that the rotor thermal deflection at the overhung node was proportional to the journal midspan ΔT, regardless of the detailed rotor geometry and the temperature distribution [11,12,14,15,17,30]. A more accurate second group [20,21] employed the 3D FEA to predict the rotor thermal bow at the rotor overhung nodes. Note that both groups neglect the rotor thermal bow between bearings, which could lead to incorrect ME responses [23,31]. The current analysis applies a "hybrid FEA" to a general dual-bearing rotor system with a double-overhung configuration to predict the entire rotor thermal bow profile at both the rotor midspan and the overhung locations.

Fig. 3 illustrates the schematics of the hybrid FEA, which is proposed to ensure high computational efficiency in the 3D transient analysis without sacrificing accuracy. The 3D brick elements are adopted to accurately predict the rotor thermal expansion close to the FPTPJBs, by prescribing the rotor temperature distribution from the thermal solver. The remaining rotor sections experience almost negligible asymmetric temperature rise and are therefore simplified with beam element models. Each node in the brick element has three degrees of freedom (DOFs), i.e., x, y, z displacements, and each node in the beam has six

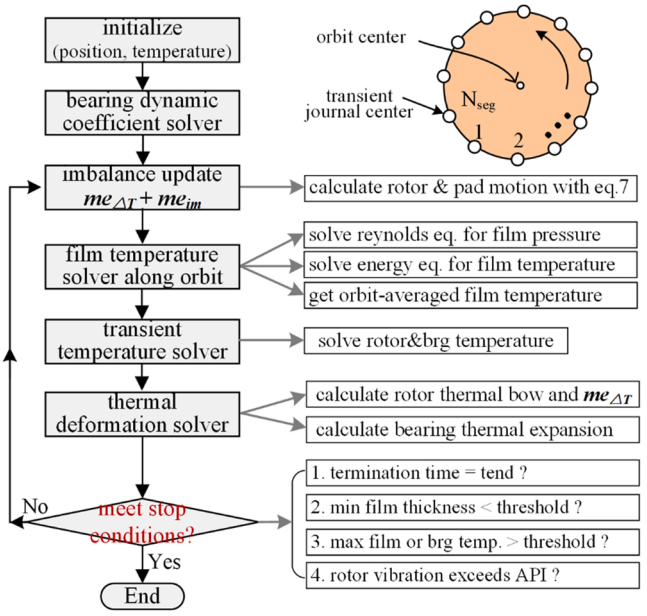

Fig. 4. Workflow of the FPTPJB Morton effect algorithm.

DOFs, i.e., three displacements and three angles. Fictitious beams are designed to connect the 3D brick elements and the beam elements to ensure displacement and rotation continuity at the rotor center, especially for the hollow rotor with no center node. The connecting beams also transmit the bending moment due to the asymmetric radial expansion of the thermal rotor. In the FEA solver, the global mass and stiffness matrices from both beam and solid elements are assembled, and the thermal loadings are applied to the brick elements to evaluate the entire rotor thermal deflection. An exaggerated example is provided at the bottom of Fig. 3 to illustrate a bowed rotor profile, and more realistic thermal bow cases are presented in Section 5.

3.2. Equivalent Thermal Imbalance

The rotor thermal bow is modeled with the distributed thermal imbalance, as shown in Eq. (6), where, $me_{\Delta T,xn}$ and $me_{\Delta T,yn}$ are the x, y components of the distributed thermal imbalance at the nth node, m_n is the nodal mass, $e_{\Delta T,n}$ and $\varphi_{\Delta T,n}$ are the nodal amplitude and phase of the rotor thermal bow, ω is the rotor spinning speed.

$$\left\{\begin{array}{l} me_{\Delta T,xn} = m_n e_{\Delta T,n}\cos(\omega t+\varphi_{\Delta T,n}) \\ me_{\Delta T,yn} = m_n e_{\Delta T,n}\sin(\omega t+\varphi_{\Delta T,n}) \end{array}\right\} \tag{6}$$

The total imbalance of the rotor-bearing system is the linear superposition of the thermal imbalance vector $\boldsymbol{me}_{\Delta T}$ and the mechanical imbalance vector $\boldsymbol{me}_{im}$. The rotor and pad dynamics vector $\boldsymbol{U}$ consisting of the rotor displacements and the pad modal components at each time step is calculated based on Eq. (7), where $\boldsymbol{M}$, $\boldsymbol{C}$, $\boldsymbol{K}$ are the global mass, damping and stiffness matrices consisting of the rotor components and the FPTPJB dynamic coefficients in the pad modal coordinate. Note that performing the FPTPJB dynamic coefficient prediction is the prerequisite of the ME analysis in the current research, and the detailed workflow will be discussed in Section 4.1. For the sake of brevity, the matrix assembly process of $\boldsymbol{M}$, $\boldsymbol{C}$, $\boldsymbol{K}$ is skipped, and interested readers could refer to Ref [21] for details.

$$\boldsymbol{U}(i\omega) = (-\omega^2\boldsymbol{M}+j\omega\boldsymbol{C}+\boldsymbol{K})^{-1}(\omega^2\boldsymbol{me}_{\Delta T}+\omega^2\boldsymbol{me}_{im}) \tag{7}$$

Where $\boldsymbol{me}_{\Delta T}$ is not necessarily in phase with $\boldsymbol{me}_{im}$.While $\boldsymbol{me}_{im}$ remains constant throughout the simulation, $\boldsymbol{me}_{\Delta T}$ usually starts from zero and gets updated by the rotor thermal bow in the time domain. In fact, when the ME develops, both the magnitude and phase of $\boldsymbol{me}_{\Delta T}$ may oscillate substantially, and the growing $\boldsymbol{me}_{\Delta T}$ may outweigh $\boldsymbol{me}_{im}$, causing severe synchronous vibration, or even diverging spiral vibration in the 1X polar plot. During the rotor coast-down process, the rotor temperature typically cannot recover fast enough and thus lags the spinning speed. The residual thermal imbalance induced by the ME usually causes hysteresis in vibration, i.e., the coast-down vibration level is higher than the run-up at the same rotor speed. All these are typical signs of ME instability problems.

Table 1
Bearing parameters tested by Al-Ghasem and Childs.

Parameter	Value
Pad number & Arc angle	4 & 72°
Pad axial length	76.2 mm
Offset	0.5
Shaft radius	58.4 mm
Bearing & Pad clearance	165 & 254 μm
Web thickness & height	2.13 & 7.44 mm
Lubricant viscosity	VG32
Supply oil temperature	38 ℃
Load type	LBP
Unit load	517, 1034 KPa

4. Algorithm for the ME analysis and experimental benchmark

4.1. Overall workflow

The flowchart of the ME prediction in the FPTPJB system is illustrated in Fig. 4. Multiple steps are involved: (1) the initial rotor/bearing temperature and position are set, (2) the dynamic coefficient solver performs the TEHD analysis with the 3D FEA to calculate the equilibrium position and the dynamic coefficient matrices in the pad modal coordinate. The dynamic coefficients are then assembled into the global $\boldsymbol{M}, \boldsymbol{C}, \boldsymbol{K}$ together with the pad modal mass and rotor components, (3) the system imbalance is updated by adding the $\boldsymbol{me}_{\Delta T}$ and $\boldsymbol{me}_{im}$, and Eq. (7) is applied to predict the synchronous journal orbit and the pad motion in the vector $\boldsymbol{U}(i\omega)$, (4) the journal/pad cycle is divided into N_{seg} segments both spatially and temporally, and the fluid film temperature field is determined at the end of each segment and then is orbit-averaged to get the temperature and heat flux at the pad/film and journal/film interfaces. Note that the orbit averaging process is performed in the shaft rotating frame to obtain the journal/film boundary conditions, which are different from the pad/film interface, as the pad/film boundary conditions can be conveniently done in the stationary frame. N_{seg} is set to be 40 in the following analysis to ensure a converged journal/pad temperature, (5) the transient rotor and bearing temperature are predicted based on the updated thermal boundary conditions at the interfaces, (6) the rotor thermal bow is predicted with the hybrid FEA following step 5 to update the equivalent thermal imbalance, and the journal/bearing thermal expansion is predicted with the 3D FEA to update the film thickness, (7) "stop" conditions are checked to determine whether additional time steps are needed. If yes, the system imbalance will be updated, and the algorithm will proceed to the next time step by restarting from step 3.

4.2. Benchmark by the measured bearing dynamic coefficients

Al-Ghasem and Childs [3,4] conducted experiments to measure the dynamic coefficients of a four-pad FPTPJB over a range of speeds and loadings, as listed in Table 1. The measurements are used to benchmark the proposed FPTPJB TEHD module in terms of dynamic coefficients and bearing temperature.

Al-Ghasem [4] mentioned that the bearing was "crushed" during assembly with different diametral clearances, resulting in asymmetric direct stiffness and damping coefficients in two orthogonal directions. Given that the clearance asymmetry is beyond our focus, the case is

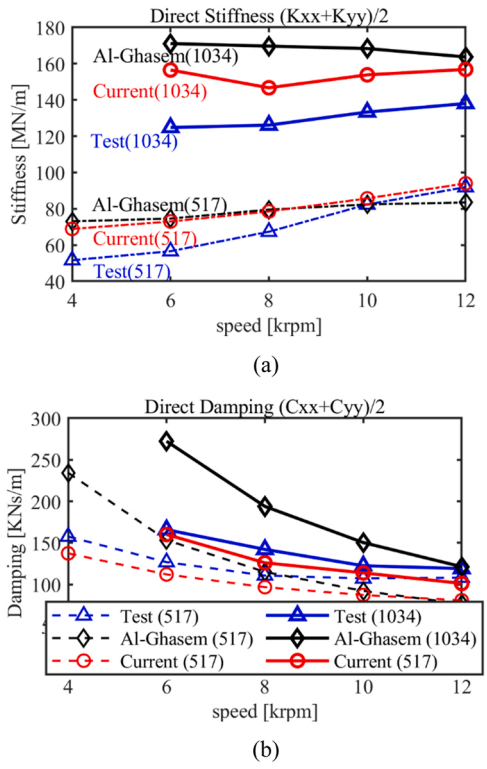

Fig. 5. Comparison of the average (a) direct stiffness and (b) direct damping coefficients at unit loads of 517 and 1034 KPa.

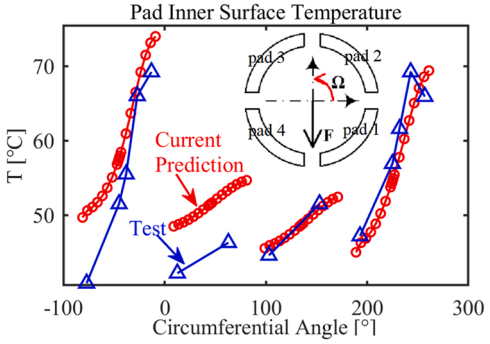

Fig. 6. Pad temperature comparison at 12,000 rpm and 1034 KPa.

assumed symmetric in the following analysis, therefore generating almost identical direct stiffness and damping in both directions. This same assumption was also adopted in Al-Ghasem's prediction model. The experimental measurements of K_{xx} and K_{yy}, C_{xx} and C_{yy} are averaged to plot against the predictions of Al-Ghasem [4] and the current analysis in Fig. 5. Note that both predictions correctly reflect the decreasing trend of the direct damping and the increasing trend of the direct stiffness with the rotor speed under both loading conditions. Meanwhile, Al-Ghasem overpredicts the direct stiffness and damping, especially at the lower speed, by more than 40 %. The current analysis slightly underpredicts the direct damping and overpredicts the direct stiffness, and the results are reasonably closer to the measurements. Fig. 6 compares the measurements [3] and the predicted pad inner surface temperature at the bearing midspan. The bottom two loaded pads are hotter than the other two pads on the top and the predictions agree reasonably well with the measurements. Note that the film thickness is usually smaller near the loaded pad and thus intensifies the oil viscous shearing. The second pad is recorded with the lowest temperature in the experiment, while the current analysis overpredicts its

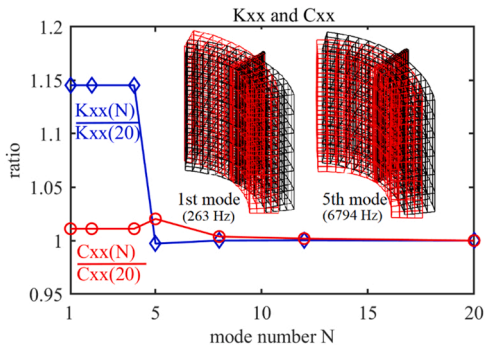

Fig. 7. Predicted K_{xx} and C_{xx} with different mode numbers at 12 krpm and 1034 KPa.

Table 2
Bearing configuration tested by Plantegenet.

Parameter	Value
Pad number & Arc angle	4 & 72°
Pad axial length	30 mm
Offset	0.6
Shaft radius	22.5 mm
Bearing & Pad clearance	50 & 75 μm
Web thickness & height	0.75 & 2.5 mm
Lubricant viscosity	VG32
Supply oil temperature	24 ℃
Load type	LBP
Load	175 N

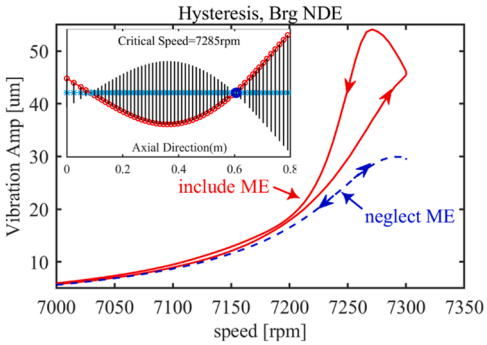

Fig. 8. Vibration Hysteresis caused by Morton effect.

temperature by about 6 ℃. The discrepancy could be due to the "crushed" bearing assembly with asymmetric bearing clearances and will be investigated in the future. Overall, the proposed algorithm provides satisfactory accuracy in predicting the bearing temperature and dynamic dynamics.

The number of flexible pad modes in the modal truncated dynamics solver plays a significant role in balancing the accuracy and the computational cost. Generally, more modes yield better accuracy by sacrificing efficiency. Unnecessary modes of very high frequencies are not excited and contribute little to accuracy. Fig. 7 illustrates the K_{xx} and C_{xx} (K_{yy} and C_{yy} are almost symmetric) at various mode number N by benchmarking with the converged $N = 20$ case. Note that the 1st mode, i.e., the tilting mode, and the 5th mode, i.e., the bending and pivot translational mode, dominate the accuracy curves. When $N > 10$, the predicted K_{xx} and C_{xx} stabilize with negligible changes. Therefore, all analysis in the current manuscript is conducted based on $N = 10$ unless specified otherwise.

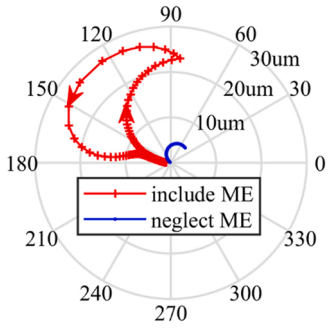

Fig. 9. 1X Polar plot at the bearing NDE.

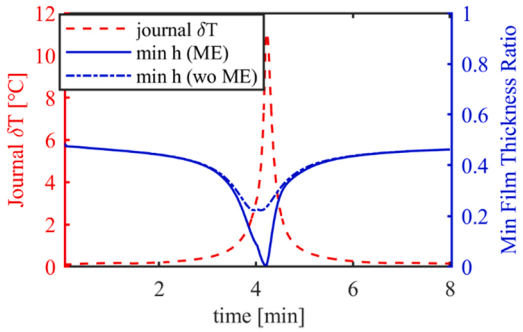

Fig. 10. Journal ΔT and minimum film thickness ratio.

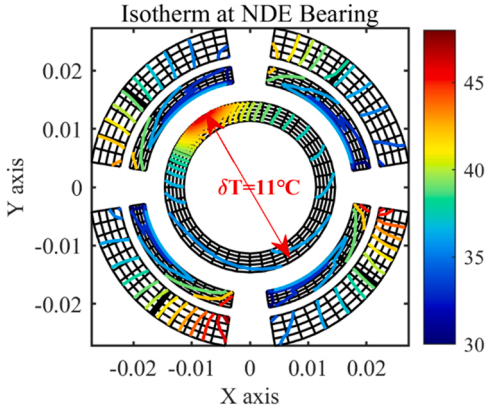

Fig. 11. Bearing isotherms at t = 4 min, 13 s during rotor coasts down.

4.3. Benchmark by the Morton effect experiment

Plantegenet and Arghir built a testing rig to investigate the FPTPJB ME, with parameters listed in Table 2 and detailed rotor geometries in Ref [27]. The predicted critical speeds with the current TEHD analysis are found to be 6.3 krpm and 7.3 krpm, and the latter one has a forward mode with a damping ratio less than 5 %, which agrees with the descriptions in Ref [27]. The experimental observations are hereby used to verify the proposed ME algorithm.

During simulation, the rotor speed is set to linearly increase from 6600 rpm to 7300 rpm within 4 mins and then decrease back to 6600 rpm within another 4 mins. Fig. 8 illustrates the hysteresis phenomenon viewed at the bearing NDE (Non-drive-end) side. Note that the rotor coast-down vibration is clearly higher than the run-up, and simply neglecting the ME by setting the thermal imbalance to zero sees a significant reduction in the vibration amplitude, and the hysteresis also disappears. The hysteresis vibration is a clear sign of the thermal bow-induced phenomenon. Note that the journal has a large thermal mass,

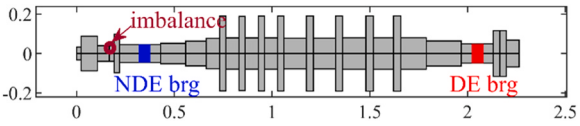

Fig. 12. Double-overhung rotor configuration.

Table 3
Bearing parameters of the double-overhung compressor.

Parameter	Value
Pad number & Arc angle	5 & 56°
Pad axial length	49 mm
Offset	0.5
Shaft radius	49 mm
Bearing & Pad clearance	73.5 & 147 μm
Web thickness & height	2 & 6 mm
Lubricant viscosity	VG32
Supply oil temperature	50 ℃
Load type	LOP
Load	2400 N
Mechanical imbalance	1.4E-4 kg.m

and its thermal change usually lags the rotor speed. During the coast-down process, the journal ΔT and the rotor thermal bow cannot recover fast enough, and the residual thermal imbalance gives a different excitation compared with the rotor run-up, causing the hysteresis phenomenon. Fig. 9 illustrates the 1X polar plot viewed at the FPTPJB NDE, note that the ME has greatly amplified the vibration, and neglecting the ME significantly underpredicts the rotor transient response.

Fig. 10 illustrates the minimum film thickness ratio h/C_b and the peak-peak journal ΔT. Note that the minimum film thickness drops to almost zero when the rotor speed barely decreases from the peak speed of 7300 rpm, when the maximum journal ΔT is also observed. Neglecting the ME incorrectly raises the minimum film thickness ratio above 20 %, and falsely indicates synchronous vibration stability. Fig. 11 gives a snapshot of the bearing isotherms at t = 4 min 13 s. Note that the journal ΔT reaches 11 ℃, and the hot spot is clearly visible with the cold spot located almost out of phase. Overall, the proposed algorithm successfully predicts the ME in Plantegenet's system, with a clear hysteresis vibration and large journal ΔT, which were also observed in the experiment [27].

5. Morton effect discussion based on a real compressor

The FPTPJB in Section 4.3 with a relatively small dimension and a light load experimentally demonstrated that the FPTPJB is prone to the ME instability under certain conditions. Nevertheless, a real-world ME problem induced by the FPTPJBs of industrial size and load will be more convincing. Unfortunately, such industrial cases are very rare given the relatively more recent application of FPTPJBs compared with the classic tilting pad bearings. Thereby, deJongh and Morton's compressor in Fig. 12 is selected for the theoretical modeling. The original compressor was supported by two tilting pad bearings and had a double-overhung arrangement [17]. During testing, it was found impossible to achieve the maximum continuous speed around 11.9 krpm due to the large spiral vibration. The original system has been thoroughly investigated in earlier publications [21,22]. In the following analysis, the original bearings are replaced with two similar FPTPJBs in Table 3. The pad and the thermal rotor are meshed by 21 × 5 × 6, 40 × 6 × 14 layers in the circumferential, radial, and axial direction, respectively, to ensure a converged transient ME response. The entire algorithm is implemented by the mixing programming of C and Matlab to accelerate the simulation, and the "ode15s" method is chosen in Matlab to solve the dynamics and thermal differential equations with the relative tolerance of 1E-3 and absolute tolerance of 1E-4 to balance the accuracy and efficiency.

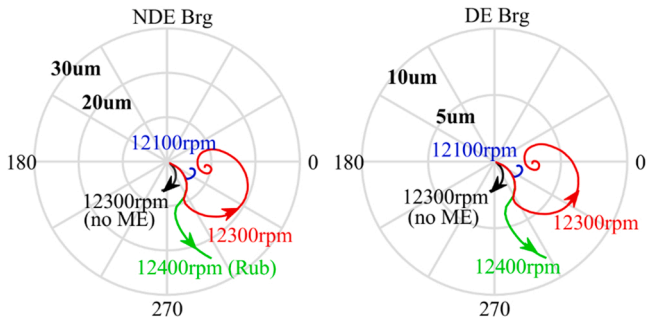

Fig. 13. 1X polar plot at various target speeds.

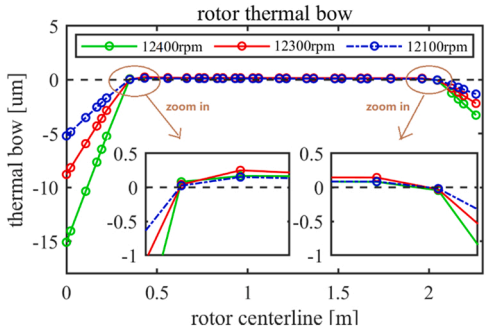

Fig. 14. Rotor thermal bow profile at various target speeds.

All simulations are done on a workstation with 8 CPUs of 3 GHz and 16 GB memory and each case takes about 4 h to complete the 4-min simulation on average.

5.1. Morton effect of FPTPJBs at various rotor speed

All FPTPJB parameters in Table 3 are identical to the tilting pad bearings in Ref [17,21], except the FPTPJB web thickness and height, which are set based on a typical industrial application, and hereby serve as the benchmark unless specified otherwise. Variations of the web thickness will be allowed for parametric studies in Section 5.3. In all cases, the rotor speed increases linearly from 9 krpm to the target speed within one minute and keeps constant until the termination time of 4 mins is reached, given that each ME spiral cycle usually takes several minutes.

During simulations, the DE (drive-end) bearing in Fig. 12 experiences relatively minor ME compared with the NDE bearing, i.e., smaller journal ΔT and rotor thermal bow and thus a lower vibration amplitude. Fig. 13 illustrates the 1X polar plot at various target speeds, note that the vibration amplitude of the DE bearing is much smaller than the NDE. By increasing the rotor speed from 12,100 rpm to 12,400 rpm, the rotor vibration grows larger, until "dry rub" occurs at 12,400 rpm for the NDE bearing and the simulation is terminated. The rotor speed of 12,300 rpm sees a clear spiral vibration in the 1X polar plot, and even at a constant speed, the journal vibration keeps oscillating in both amplitude and phase, and this is a typical indicator of the ME. Excluding the ME at 12,300 rpm results in the simulation significantly under-predicting the journal vibration. Fig. 14 plots the rotor thermal bow profile, and it is evident that the thermal bows at the overhung nodes dominate the overall thermal deflection profile, with almost negligible bow components in the rotor midspan. Increasing the rotor speed from 12,100 rpm to 12,400 rpm, results in the rotor thermal bows at the overhung nodes increasing monotonically, indicating that the ME grows stronger. The DE rotor side sees a smaller thermal bow amplitude, indicating that the ME is more severe on the NDE bearing side, which is consistent with Fig. 13. Therefore, only the NDE journal/bearing will be discussed in the following sections. Fig. 15 plots the sum of the distributed thermal imbalance components, which are the nodal masses multiplied by the corresponding thermal bows (recall Eq. 6). Note that the thermal imbalance keeps changing at constant speed in both phase and amplitude and exceeds the original mechanical imbalance when the ME grows stronger. Therefore, the total imbalance, i.e., the vector sum of the thermal and mechanical imbalance, excites a spiral vibration, as seen in Fig. 13.

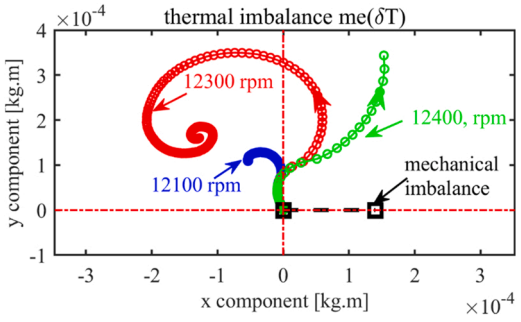

Fig. 15. Equivalent thermal imbalance at various target speeds.

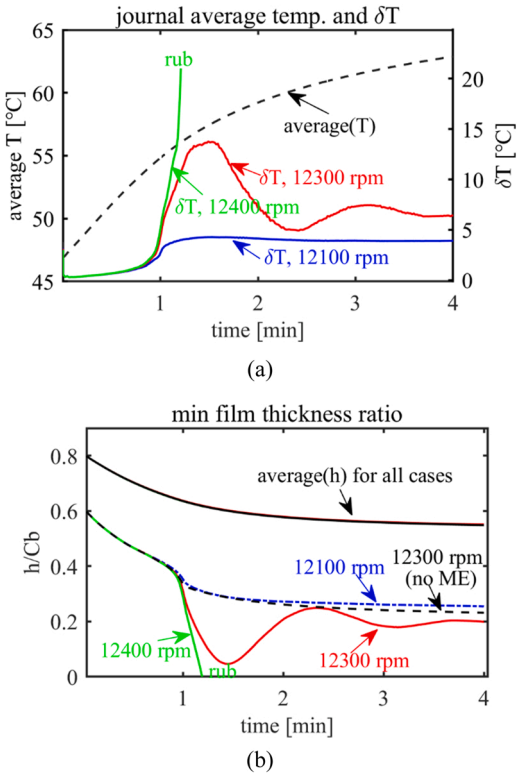

Fig. 16. Morton effect response at various target speeds at the NDE bearing (a) journal average temperature and journal ΔT (b) minimum film thickness ratio.

Fig. 16 shows the predicted ME response at various target speeds. Note that in Fig. 16(a), while the average temperature barely changes at various rotor speeds, the transient journal ΔT grows significantly at a higher speed, indicating a much stronger ME. The ΔT at 12,300 rpm oscillates in the time domain, leading to a changing thermal imbalance and spiral vibration, which also justifies why the minimum film thickness fluctuates at 12,300 rpm in the time domain. The journal ΔT at 12,400 rpm exceeds 20 ℃ and triggers large vibration with the minimum film thickness dropping to almost zero in the NDE bearing in Fig. 16(b), indicating that a "dry rub" occurs between the journal and the bearing. The reduction of the average film thickness is due to the

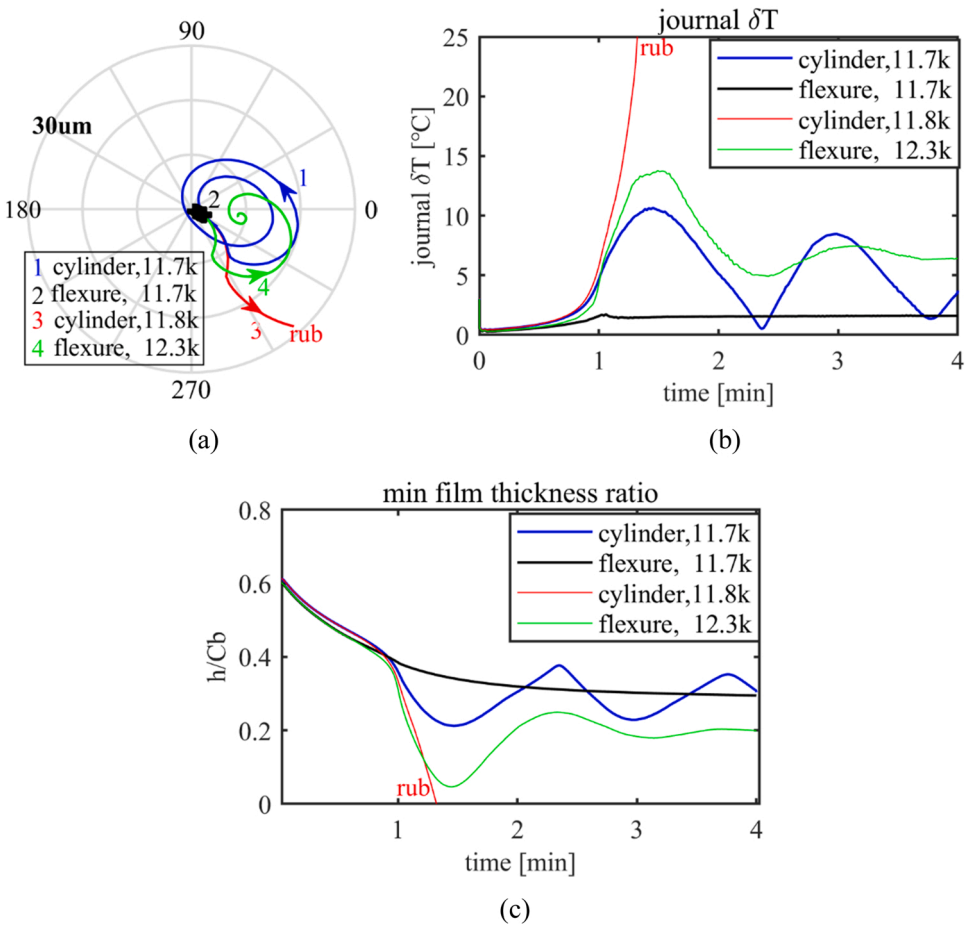

Fig. 17. Comparison of Morton effect response between the flexure-pivot and cylindrical-pivot bearing (a) 1X polar plot (b) journal ΔT (c) minimum film thickness ratio.

increased average journal and bearing temperature, which expands the solids and results in a smaller hot bearing clearance.

5.2. Comparison between the flexure and the cylindrical pivot

Given that the original compressor was supported by two tilting pad bearings with the cylindrical pivot [17,21], Fig. 17 compares the ME response with the flexure pivot and the cylindrical pivot tilting pad bearings. At 11.7 krpm, the cylindrical-pivot bearing observes a much stronger spiral vibration than its flexure-pivot companion in Fig. 17(a). Fig. 17(b) shows that at 11.7 krpm, the journal ΔT supported by the cylindrical pivot bearing reaches as high as 10 ℃ and fluctuates in the time domain, while the journal ΔT in the flexure-pivot bearing system remains at a low level. By increasing the rotor speed to 11.8 krpm, the spiral vibration of the cylindrical-pivot bearing system diverges, and the journal ΔT exceeds 25 ℃, indicating that the ME is intensified, and the induced large vibration significantly diminishes the minimum film thickness ratio to almost zero, as shown in Fig. 17(c).

The predicted result agrees with the description in Ref [17] that "*it was impossible to achieve the rated maximum continuous speed of 11, 947 rpm, because of high synchronous vibration levels of the rotor*". By contrast, the prediction also shows that the FPTPJBs still operate stably up to 12.3 krpm, meanwhile, the 1X spiral becomes clearly visible and the journal ΔT reaches almost 15 ℃ and the minimum film thickness ratio drops below 10 %, all indicating that the system approximates the ME instability onset speed and any major speed increase may trigger the "dry rub". Fig. 17 shows that compared with the classical cylindrical-pivot bearing, the flexure-pivot configuration helps to increase the ME threshold speed from 11.8 krpm to over 12.3 krpm. The shifting of the threshold speed is partially attributed to the change of the critical speed, which is featured with a large overhung deflection in its mode shape [9,22] and thus easily generates a large thermal imbalance. According to the critical speed analysis, replacing the original cylindrical-pivot bearing with the flexure-pivot type increases the critical speed of the 2nd bending mode by more than 500 rpm, which helps to increase the ME instability onset speed.

5.3. Web thickness

The web thickness of the flexure-pivot plays an important role in affecting the bearing dynamic coefficients and the rotordynamics response. In this section, the default web thickness of 2 mm is compared with the thinner case of 1 mm and the thicker case of 4 mm to investigate its influence on the ME response. Web thickness beyond this range is considered less realistic and is not discussed. At 12.1 krpm, the 1 mm web sees an evident spiral vibration in the 1X polar plot in Fig. 18(a), and the maximum journal ΔT reaches over 10 ℃ in Fig. 18(b), both indicating a strong ME near the instability threshold speed. Further raising the rotor speed to 12.2 krpm substantially intensifies the ME with the diverging spiral vibration and "dry rub", as shown in Fig. 18(c). Meanwhile, both the default case of 2 mm web and the thicker case of 4 mm operate stably at 12.1 krpm, with a small vibration amplitude, journal ΔT lower than 5 ℃, and minimum film thickness ratio over 30 %. The instability threshold speed for the 2 mm and the 4 mm cases exceed 12.3 krpm and 12.4 krpm, respectively, demonstrating that a larger web thickness can effectively increase the ME instability threshold speed.

Fig. 19 compares the enlarged pad deformation at 12.1 krpm

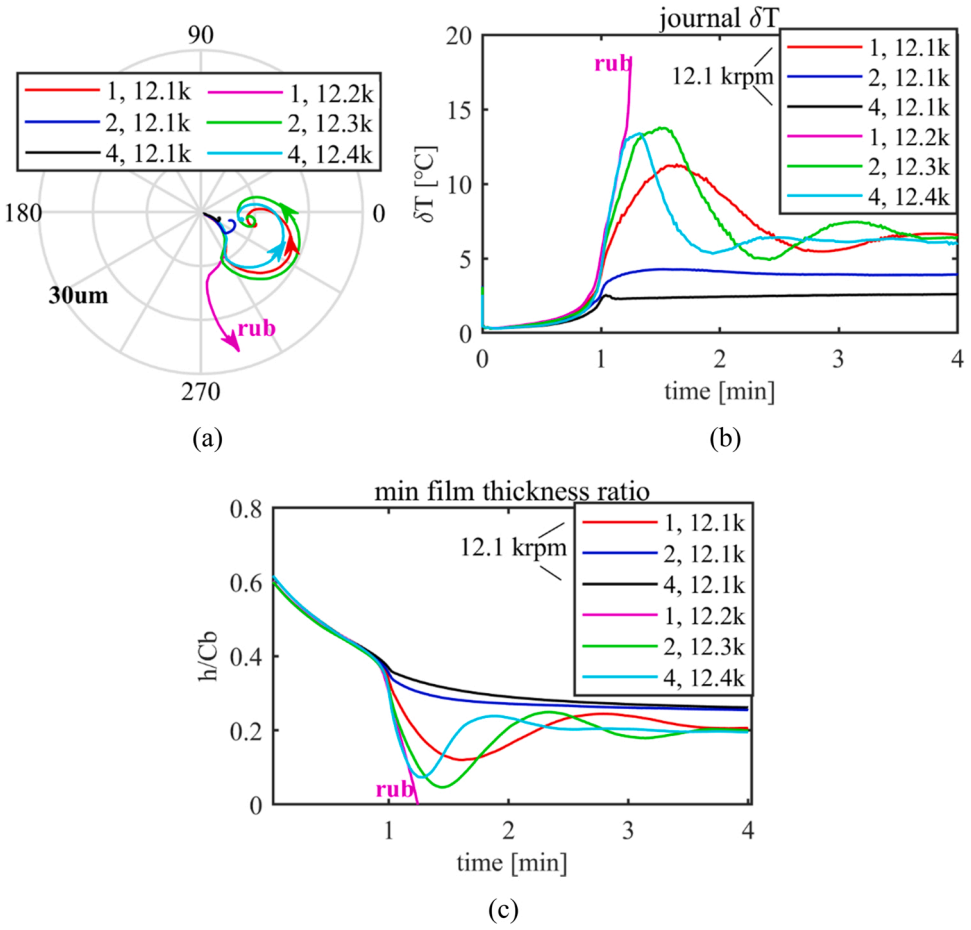

Fig. 18. Morton effect response with various web thickness for the flexure-pivot (a) 1X polar plot (b) journal ΔT, (c) minimum film thickness ratio.

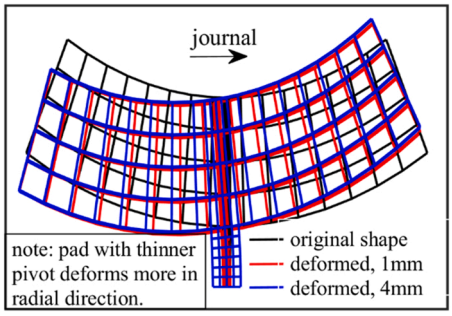

Fig. 19. Comparison of pad deformation between web thickness of 1 mm and 4 mm at 12.1 krpm.

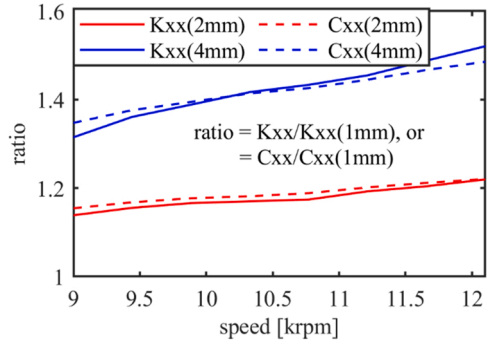

Fig. 20. Comparison of direct stiffness and damping for various web thickness cases.

between the 1 mm and 4 mm web cases. Both cases display a clear pad tilting motion, nevertheless, the pad sinks more radially in the 1 mm web case due to a larger web compression. Fig. 20 plots the ratio of K_{xx} and C_{xx} for the 2 mm and 4 mm web cases by comparing them to the 1 mm case. Increasing the web thickness from 1 mm to 4 mm stiffens the web and increases the direct stiffness and damping (K_{yy} and C_{yy} follow a similar trend). A similar conclusion was also drawn in Ref [5], where the direct dynamic coefficients of a comparable FPTPJB grew by 10 % when the web thickness increased from 2 mm to 4 mm. Thickening the flexure pivot can raise the concerning critical speed with large overhung deflections in the mode shape (in this case, it is the 2nd bending mode), therefore, shifting the ME instability onset speed accordingly.

5.4. Supply oil temperature

Considering the ME is a thermally induced instability problem, adjusting the supply oil temperature can potentially mitigate or intensify its behavior. Fig. 21 compares the temperature distribution at the bearing-journal midspan with the supply oil temperature at 40 ℃ and 50 ℃. Despite a lower average temperature of the fluids and solids at a supply oil temperature of 40 ℃, the journal isotherms are more eccentric compared with the 50 ℃ case, indicating a larger journal ΔT and a stronger ME. Fig. 22(a) shows that the polar plot diverges when the supply oil temperature is 40 ℃, leading to the "dry rub" problem. Fig. 22 (b) illustrates that the average temperature of the solids effectively drops by reducing the supply oil temperature from 50 ℃ to 40 ℃ (see line 2, 5

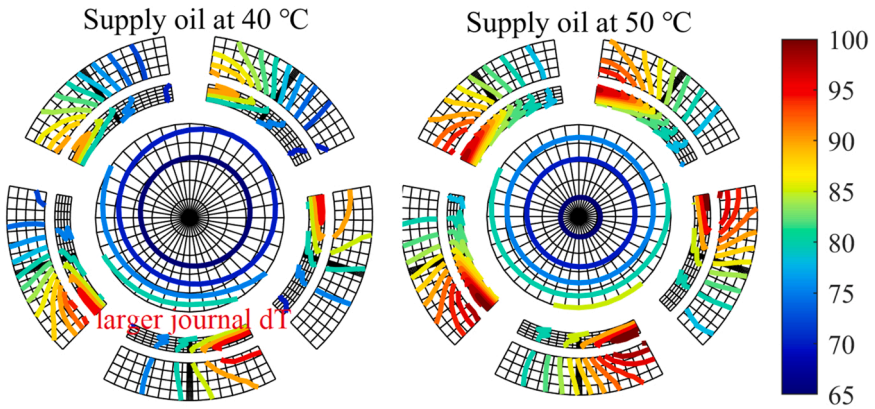

Fig. 21. Journal midspan isotherms at t = 72 s, 12.3 krpm with the supply oil temperature of 40 ℃ and 50 ℃.

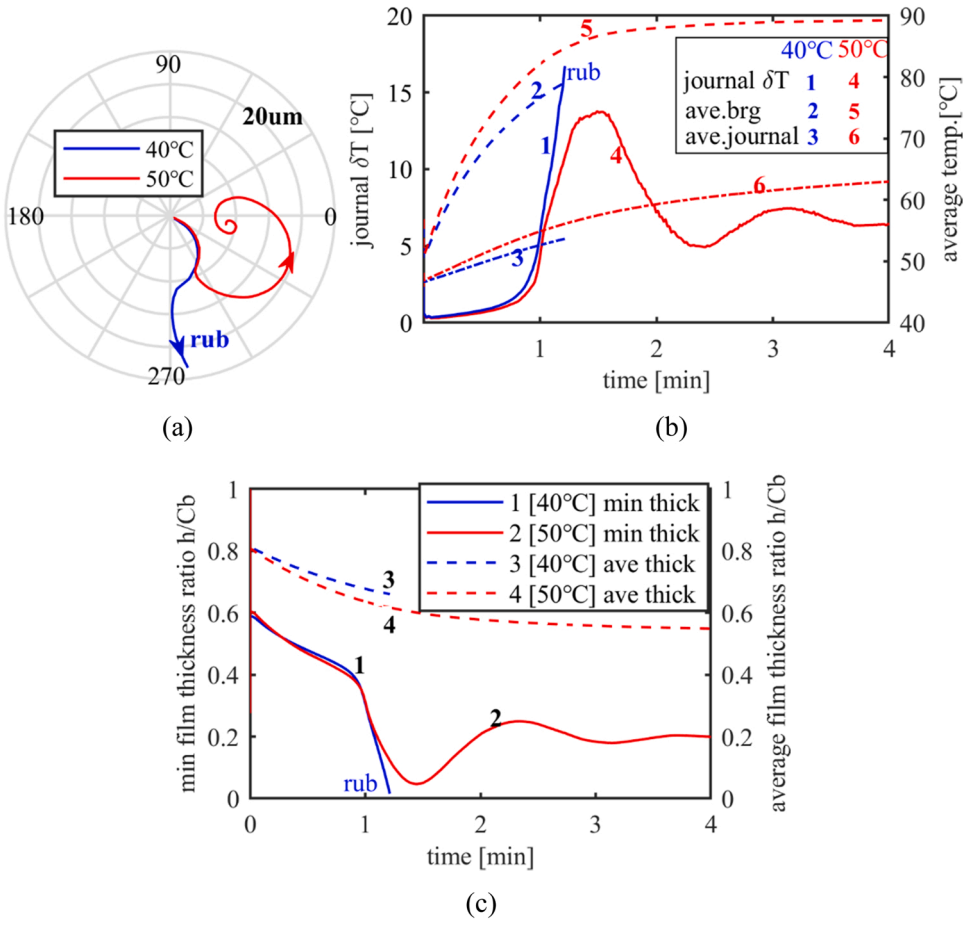

Fig. 22. Morton effect response at 12.3 krpm with various supply oil temperatures (1) 1X polar plot (b) differential and average temperature of journal and bearing (c) minimum and average film thickness ratio.

and 3, 6 by referring to the right Y-axis in Fig. 22(b)), which decreases the thermal expansion and thus increases the average film thickness in Fig. 22(c). Nevertheless, when the supply oil temperature is 40 ℃, the journal ΔT grows faster and reaches over 15 ℃ (see line 1, 4 by referring to the left Y-axis in Fig. 22(b)), and the simulation continues until the "dry rub" occurs in Fig. 22(c). A similar finding was also reported by Marscher [32], where the supply oil temperature was increased from 125 ℉ to 128℉ to suppress the high synchronous vibration induced by the ME.

For this specific rotor model, reducing the supply oil temperature is found to shift the ME instability onset speed to a lower level, which could be attributed to two factors, (1) reducing the oil temperature by 10 ℃ results in a 36 % increase in the oil viscosity, intensifying the uneven viscous heating across the journal circumference, (2) the relatively larger bearing clearance amid the cooler supply oil reduces the bearing dynamic coefficients and the rotor critical speed. Both factors contribute to the decreased ME instability onset speed with the cooler supply oil.

5.5. *Neglecting the thermal bow in the rotor midspan?*

Based on Fig. 14, readers may easily conclude that the rotor thermal

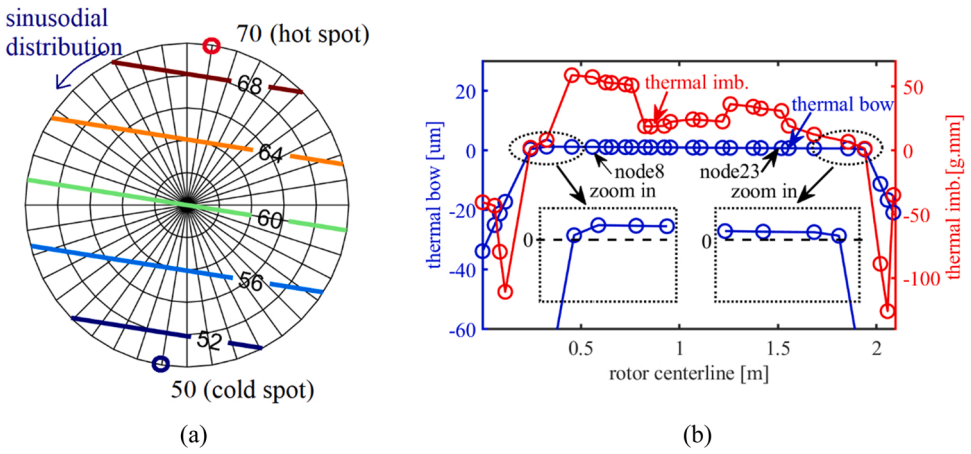

Fig. 23. Journal temperature and rotor thermal bow (a) journal temperature (b) thermal bow and thermal imbalance.

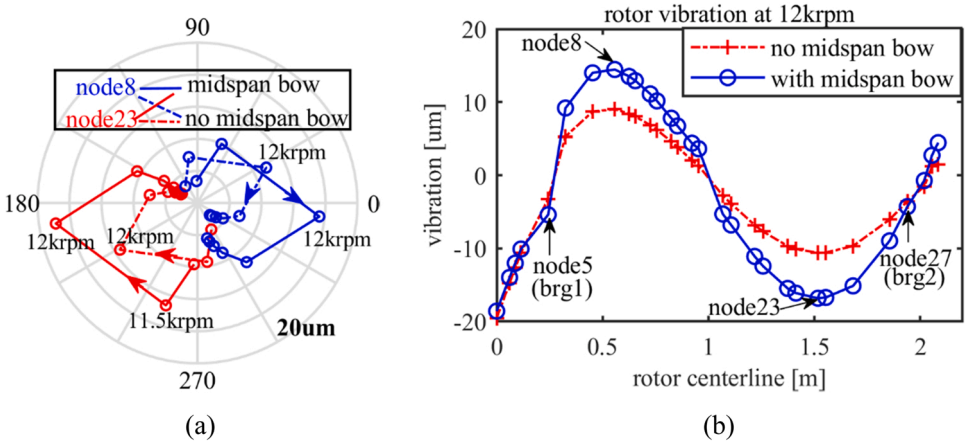

Fig. 24. Comparison of Morton effect response including/excluding the rotor midspan bow (a) 1X polar plot at node 8 and node 23 (b) rotor vibration at 12 krpm.

bow between bearings is negligible due to its small amplitude, and thus it is unnecessary to compute the thermal deflection of the entire rotor, as assumed by most earlier research. *Is it accurate to neglect the thermal bow at the rotor midspan in the Morton effect analysis*? To answer this question, several new disks are added onto the rotor midspan to increase the nodal masses, and a sinusoidal temperature field is imposed onto the journal circumference, as shown in Fig. 23(a). The rotor temperature outside the bearing span is assumed to be 50 ℃. The corresponding thermal bow and the thermal imbalance are calculated in Fig. 23(b). Despite a relatively smaller bow amplitude between bearings, the thermal imbalance in the rotor midspan is comparable to the overhung locations due to the added masses. Fig. 24(a) illustrates the vibration at node 8 and node 23 by increasing the steady rotor speed from 11 krpm to 14.5 krpm with 500 rpm apart. Fig. 24(b) presents the rotor vibration at 12 krpm with the corresponding thermal imbalance plus the mechanical imbalance. Note the significant discrepancy if the rotor midspan bow is excluded, which under-predicts the ME-induced vibration by over 30 %. Although the ME cases are overwhelmingly reported in the overhung turbomachinery, the thermal bow between bearings could substantially affect the rotordynamics, and therefore simply excluding the thermal bow at the rotor midspan could lead to significant errors in predicting the ME response.

6. Conclusion

FPTPJBs have widespread applications for industrial turbomachinery, and the presented results clearly demonstrate the potential for a Morton effect occurrence in these critical machines. The Morton effect cannot be predicted by the classical rotordynamics software due to its coupled thermo-elasto-hydrodynamic-rotordynamic nature, as underscored by the API [10]. The current research presents a TEHD bearing model with pad and web flexibility and a rotor thermal bow algorithm, both of which are successfully benchmarked by correlation with experimental data. The unique contribution of the current research includes a comprehensive Morton effect analysis based on a realistic double-overhung compressor by replacing the original tilting pad bearings with the FPTPJBs. The main takeaways are summarized below.

(1) Theoretical predictions have confirmed the propensity of the FPTPJB system to experience the Morton effect, with symptoms including spiral vibration, hysteresis phenomenon, and sensitivity to operating conditions.
(2) Even with similar bearing parameters, the FPTPJBs and the classical tilting pad bearings can lead to different Morton effect instability onset speeds.
(3) Increasing the web thickness from 1 mm to 4 mm and increasing the supply oil temperature from 40 ℃ to 50 ℃ mitigated the Morton effect in the case presented.
(4) Neglecting the thermal bow in the rotor midspan may result in incorrect predictions of the Morton effect response.

Future work involves enhancing the TEHD bearing model, by expanding the thermal boundary conditions to include heat conduction between the web and the bearing shell. More importantly, a more

advanced asymmetric oil-mixing model by taking account of the loading, speed, and bearing configuration, will be proposed to accurately predict the oil temperature distribution at the pad inlet, and to evaluate the supply oil temperature influence on the Morton effect response.

Statement of originality

As corresponding author, I Yan Shi, hereby confirm on behalf of all authors that:

1) The paper has not been published previously, that it is not under consideration for publication elsewhere, and that if accepted it will not be published elsewhere in the same form, in English or in any other language, without the written consent of the publisher.

2) The paper does not contain material which has been published previously, by the current authors or by others, of which the source is not explicitly cited in the paper.

Declaration of Competing Interest

The authors declare that they have no known competing financial interests or personal relationships that could have appeared to influence the work reported in this paper.

Data availability

No data was used for the research described in the article.

Acknowledgements

The work described in this paper was supported by National Natural Science Foundation of China (Grant No. 12202026), Outstanding young scientists in Beijing (Grant No. BJJWZYJH01201910006021).

References

[1] San Andres L, Flow Turbulent. Flexure-pivot hybrid bearings for cryogenic applications. J Tribol 1996;118(1):190–200.
[2] Kepple W, Read D, Zeidan F, Paraskevakos C, Dawson M. Experience in the use of flexure pivot tilt pad bearings in boiler feed water pumps. In: Proceedings of the fifteenth int. pump user symp.; 1998.
[3] Al-Ghasem AM. Measurement of rotordynamic coefficients for a high-speed flexure pivot tilting-pad bearing (load between pad) configuration [Thesis] Texas A&M University; 2005.
[4] Al-Ghasem AM, Childs DW. Rotordynamic coefficients measurements versus predictions for a high-speed flexure-pivot tilting-pad bearing (load-between-pad configuration). J Eng Gas Turbines Power 2006;128(4):896–906.
[5] Suh J, Palazzolo A, Choi Y. Numerical modeling and analysis of flexure-pivot tilting-pad bearing. J Tribol 2017;139(5):1–13.
[6] Vannini G, Cangioli F, Ciulli E, Nuti M, Forte P, Kim J, et al. Experiments on a large flexure pivot journal bearing: summary of test results and comparison. Predict, J Eng Gas Turbines Power 2020;142(3):1–8.
[7] Hesseborn B. Measurements of temperature unsymmetries in bearing journal due to vibration. Intern Rep ABB Stal 1978.
[8] Morton PG. Some aspects of thermal instability in generators, G.E.C. Internal Report No. S/W40 u183; 1975.
[9] Tong X, Palazzolo A, Suh J. A review of the rotordynamic thermally induced synchronous instability (Morton) effect. Appl Mech Rev 2017;69(6):1–13.
[10] API. Standard No. 684. Tutorial on Rotordynamics: Lateral Critical, Unbalance Response, Stability, Train Torsional and Rotor Balancing. 2nd ed. Washington, DC: American Petroleum Institute; 2005.
[11] Keogh P, Morton P. Journal bearing differential heating evaluation with influence on rotor dynamic behaviour. Proc R Soc Lond Ser A 1913;441(1993):527–48.
[12] Keogh P, Morton P. The dynamic nature of rotor thermal bending due to unsteady lubricant shearing within a bearing. Proc R Soc Lond Ser A 1924;445(1994):273–90.
[13] Gomiciaga R, Keogh P. Orbit induced journal temperature variation in hydrodynamic bearings. J Tribol 1999;121(1):77–84.
[14] Balbahadur AC, Kirk R. Part I—theoretical model for a synchronous thermal instability operating in overhung rotors. Int J Rotating Mach 2004;10(6):469–75.
[15] Murphy B, Lorenz J. Simplified morton effect analysis for synchronous spiral instability. J Vib Acoust 2010;132(5):1–10.
[16] Lorenz J, Murphy B. Case study of morton effect shaft differential heating in a variable-speed rotating electric machine (ASME Paper No. GT2011-45228). Proc. ASME Turbo. Expo. USA: Phoenix; 2011.
[17] de Jongh F, Morton P. The synchronous instability of a compressor rotor due to bearing journal differential heating. ASME Pap No 94-GT-035 1994.
[18] D. Panara, L. Baldassarre, D. Griffin, A. Mattana, S. Panconi, E. Meli. Numerical Prediction and Experimental Validation of Rotor thermal Instability. In: Proceedings of the forty fourth turbomachinery symp.; 2015.
[19] Rindi A, Baldassarre L, Panara D, Meli E, Ridolfi A, Frilli A, et al. An efficient iterative approach for the analysis of thermal instabilities in rotating. Mach, J Vibr Acoust 2017;139(6):1–15.
[20] Suh J, Palazzolo A. Three-dimensional thermohydrodynamic morton effect simulation—part i: theoretical model. J Tribol 2014;136(3):1–14.
[21] Tong X, Palazzolo A. Double overhung disk and parameter effect on rotordynamic synchronous instability-morton effect: part i: theory and modeling approach. J Tribol 2016;139(1):1–11.
[22] Tong X, Palazzolo A. Double overhung disk and parameter effect on rotordynamic synchronous instability-morton effect: part ii: occurrence and prevention. J Tribol 2016;139(1):1–10.
[23] X. Tong, A. Palazzolo, J. Suh. Rotordynamic morton effect simulation with transient, thermal shaft bow. J Tribo., 138(3) (1016): 1–12.
[24] Shin D, Palazzolo A, Tong X. Squeeze film damper suppression of thermal bow-morton effect instability. J Eng Gas Turbines Power 2020;142(12):1–14.
[25] Tong X, Palazzolo A. Measurement and prediction of the journal circumferential temperature distribution for the rotordynamic morton effect. J Tribol 2018;140(3):1–10.
[26] Plantegenet T, Arghir M, Hassini M, Jolly P. The thermal unbalance effect induced by a journal bearing in rigid and flexible rotors: experimental analysis. Tribol Trans 2020;63(1):52–67.
[27] Plantegenet T, Arghir M, Jolly P. Experimental analysis of the thermal unbalance effect of a flexible rotor supported by a flexure pivot tilting pad bearing. Mech Syst Signal Process 2020;145:1–16.
[28] Shin D, Suh J, Palazzolo A. Parametric study of flexure pivot bearing induced thermal bow-rotor instability (Morton effect). J Tribol 2022;144(7):1–15.
[29] Tong X, Palazzolo A. Tilting pad gas bearing induced thermal bow-rotor instability (Morton effect). Tribol Int 2018;121:269–79.
[30] Lee J, Palazzolo A. Morton effect cyclic vibration amplitude determination for tilt pad bearing supported machinery. J Tribol 2013;135(1):1–12.
[31] Guo Z, Kirk G. Morton effect induced synchronous instability in mid-span rotor–bearing systems—part i: mechanism study. J Vibr Acoust 2011;133(6):1–11.
[32] Marscher W, Illis B. Journal bearing “Morton Effect” cause of cyclic vibration in compressors. Tribol Trans 2007;50(1):104–13.